

Thermal conductivity changes across a structural phase transition: the case of high-pressure silica

Hugo Aramberri,¹ Riccardo Rurali,¹ and Jorge Íñiguez²

¹*Institut de Ciència de Materials de Barcelona (ICMAB-CSIC),
Campus de Bellaterra, 08193 Bellaterra, Barcelona, Spain*

²*Materials Research and Technology Department,
Luxembourg Institute of Science and Technology,
5 avenue des Hauts-Fourmeaux, L-4362 Esch/Alzette, Luxembourg*

(Dated: June 7, 2022)

By means of first-principles calculations, we investigate the thermal properties of silica as it evolves, under hydrostatic compression, from a stishovite phase into a CaCl_2 -type structure. We compute the thermal conductivity tensor by solving the linearized Boltzmann transport equation iteratively in a wide temperature range, using for this the pressure-dependent harmonic and anharmonic interatomic couplings obtained from first principles. Most remarkably, we find that, at low temperatures, SiO_2 displays a large peak in the in-plane thermal conductivity and a highly anisotropic behavior close to the structural transformation. We trace back the origin of these features by analyzing the phonon contributions to the conductivity. We discuss the implications of our results in the general context of continuous structural transformations in solids, as well as the potential geological interest of our results for silica.

I. INTRODUCTION

The thermal properties of solids and nanostructures are attracting a growing interest, both from the fundamental standpoint and for application-driven research. The quest for low thermal conductivity materials, for instance, is one of the main challenges in the development of efficient thermoelectric devices¹, while materials with a large thermal conductivity could help overcome the problem of heat dissipation at the nanoscale, which has become one of the major hitches for nanoscaling electronic devices^{2,3}. The thermal properties of an insulating solid are governed by its lattice thermal conductivity. This physical property is determined by the lattice vibrational modes (phonons) and by the scattering processes they encounter. At structural phase transitions which are driven by soft phonons, the lattice thermal conductivity is expected to be strongly modified, since the soft mode will experience a frequency and group velocity shift which will in turn modify the allowed phonon scattering processes in the system.

In this article we investigate the thermal properties of SiO_2 close to a structural phase transition. Some theoretical works have already calculated the thermal properties from first-principles for a handful of oxides such as ferroelectric PbTiO_3 ⁴, MgO ^{5,6}, and MgSiO_3 ⁷, but none of them was studied close to a structural phase transition.

Silicon dioxide, also known as silica, is not only the most abundant compound on Earth⁸, the Moon⁹ and the terrestrial planets^{8,10}, but is also at the heart of modern day electronic devices and is widely used as a substrate in thin film growth. The phase diagram of SiO_2 is very rich, with a wide variety of silica polymorphs such as α -quartz, β -quartz, cristobalite, tridymite or coesite. In these phases Si shows a tetrahedral coordination with the surrounding O atoms. At high pressures (of the or-

der of gigapascals) the coordination of silicon in SiO_2 becomes octahedral, giving rise to the stishovite phase, the CaCl_2 -type phase, or the α - PbO_2 -type phase at even higher pressures (of the order of 100 GPa). In particular, the pressure induced phase transition from the stishovite to the CaCl_2 -type phase is considered as a paradigmatic pseudoproper ferroelastic phase transition. While the atomic structure^{11,12}, phonon band structure¹³⁻¹⁷, electronic structure¹⁸⁻²⁰, and thermodynamic potentials describing the structural phase transition^{13,21-23} have been widely studied, both experimentally and theoretically, no previous work has addressed the thermal properties of the stishovite nor the CaCl_2 -type phases. In this work we calculate the thermal properties of the stishovite and CaCl_2 -type high pressure phases of silica as a function of temperature and pressure from first principles.

II. COMPUTATIONAL METHODS

A. Density functional calculations of the interatomic force constants

We performed first-principles electronic structure calculations within density functional theory (DFT), using the Vienna Ab-initio Simulation Package^{24,25} (VASP) along with the Perdew-Burke-Ernzerhof²⁶ (PBE) implementation of the generalized gradient approximation (GGA) for the exchange–correlation functional. We employed a plane wave basis set with a 500 eV kinetic energy cutoff with the projector augmented-wave method^{27,28}. For the ground state calculations we considered the primitive cells of the stishovite and the CaCl_2 -type phases (see Figure 1) and carefully optimized the lattice vectors and the atomic position until the residual stress and the forces were smaller than 10^{-2} kbars and 10^{-6} eV/Å, respectively. The Brillouin zone (BZ) was sampled with

a converged $4 \times 4 \times 6$ Monkhorst-Pack²⁹ grid of \mathbf{k} -points. Hydrostatic pressure was applied by varying the lattice vectors as described below, and allowing the atomic coordinates to relax.

We employed the direct supercell approach to obtain the phonon band structures. In this approach the second-order interatomic force constants (IFCs) are computed directly by considering supercells of the corresponding primitive cell with small enough (0.01 Å) atomic displacements. We employed the PHONOPY software³⁰ to generate the minimal set of supercells required to obtain the IFCs, while VASP was used to compute the Hellmann-Feynman forces in these cells. The long-range corrections to the potential were included to correctly address for dipole-dipole interactions arising from longitudinal optic (LO) vibrational modes of the crystal. The supercells with atomic displacements employed to calculate the third order IFCs, which account for the three-phonon scattering processes, were generated using THIRDDORDER.PY³¹. We employed $3 \times 3 \times 4$ supercells for computing both the second and third order IFCs at each pressure, since we found this supercell size to be well converged when compared to the results for $2 \times 2 \times 3$ supercells.

B. Solution of the Boltzmann Transport Equation

The second- and third-order IFCs obtained from the DFT calculations were used to solve the linearized Boltzmann Transport Equation (BTE):

$$\mathbf{v}_\lambda \cdot \nabla T \frac{\partial n_\lambda^0}{\partial T} = \frac{dn_\lambda}{dt} \Big|_{\text{scatt.}}, \quad (1)$$

where n_λ^0 and n_λ are the phonon distribution at and out of equilibrium, respectively, \mathbf{v}_λ is the group velocity, and $dn_\lambda/dt|_{\text{scatt.}}$ is the rate of change in the phonon distribution as a result of phonon-phonon scattering. We can assume the difference between n_λ and n_λ^0 to be of the form

$$n_\lambda = n_\lambda^0 - \mathbf{F}_\lambda \cdot \nabla T \partial n_\lambda^0 / \partial T. \quad (2)$$

Then, the linearized BTE can be rewritten in the following way³¹

$$\mathbf{F}_\lambda = \tau_\lambda^0 (\mathbf{v}_\lambda + \mathbf{\Delta}_\lambda), \quad (3)$$

where \mathbf{F}_λ is the generalized mean free path, τ_λ^0 is the relaxation time of mode λ in the relaxation time approximation (RTA), and $\mathbf{\Delta}_\lambda$ gives the deviation of the solution from the RTA. By taking into account only isotopic and anharmonic phonon scattering processes, we can write τ_λ^0 as

$$\frac{1}{\tau_\lambda^0} = \Gamma_\lambda = \Gamma_\lambda^{\text{isot}} + \Gamma_\lambda^{\text{anh}}, \quad (4)$$

where the total scattering rate of mode λ , Γ_λ , is the sum of the isotopic scattering rate $\Gamma_\lambda^{\text{isot}}$ and the anharmonic

Isot.	abund. (%)	Isot.	abund. (%)
²⁸ Si	92.23	¹⁶ O	99.76
²⁹ Si	4.67	¹⁷ O	0.038
³⁰ Si	3.10	¹⁸ O	0.2

TABLE I. Stable isotopes of Si and O and their relative naturally occurring abundances.

scattering rate $\Gamma_\lambda^{\text{anh}}$. Scattering caused by isotopic disorder depends on the mass variance of the elements in the compound and was included through the model due to Tamura³², for which we employed the natural abundances of Si and O (see Table I)³³. Three-phonon scattering processes were included to account for the anharmonic scattering, which is computed directly from the third-order IFCs obtained from the DFT calculations. Higher order scattering processes were neglected, since they are expected to be important only at very high temperatures³⁴.

The BTE in the form given in Eq. (3) is solved iteratively³⁵ in a parameter-free approach as implemented in the SHENGBTE code³¹ to obtain the lattice thermal conductivity tensor

$$\kappa_\ell^{\alpha\beta} = \frac{1}{k_B T^2 \Omega N} \sum_\lambda n^0 (n^0 + 1) (\hbar \omega_\lambda)^2 v_{\alpha,\lambda} F_{\beta,\lambda}, \quad (5)$$

where α and β are the three coordinate directions x , y , and z ; and k_B , T , Ω and N are the Boltzmann constant, the temperature, the volume of the unit cell and the number of \mathbf{q} -points in the integral over the BZ, respectively. The sum runs over all the phonon modes λ , \hbar is the reduced Planck constant, and ω_λ is the phonon frequency.

For the first iteration step $\mathbf{\Delta}_\lambda$ is set to zero, which is tantamount to starting the iterative procedure from the RTA solution. The solution is considered to be converged when the relative change in all the components of the thermal conductivity tensor becomes smaller than 10^{-5} .

C. Convergence issues

The convergence tests of the relevant parameters of the electronic structure calculations –plane-wave energy cutoff, \mathbf{k} -point mesh– were carried out as usual. In the same way, we carefully checked the dependence of the IFCs on the supercell size, finding that a $3 \times 3 \times 4$ supercell yielded converged values.

Some convergence issues related to the numerical solution of the BTE must be addressed as well. The first one concerns the δ functions appearing in the energy conservation terms in the scattering rates, which are approximated by Gaussian functions for which the standard deviation is computed in a self-adaptive manner as implemented in the SHENGBTE code³¹. The locally adapted Gaussian standard deviation appearing in the computation of the scattering rates (both anharmonic and iso-

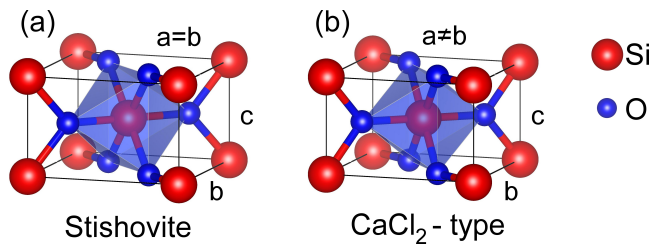


FIG. 1. Unit cell of SiO_2 in the stishovite phase (a) and the CaCl_2 -type phase (b). Si (O) atoms are shown in red (blue). The stishovite phase is a tetragonal crystal while the CaCl_2 -type phase is orthorhombic. Note that the oxygen octahedron (highlighted in blue) is tilted in the CaCl_2 -type phase.

topic) was scaled by 0.1. This scaling was necessary because unscaled standard deviations prevented to converge the solution of the BTE in a non-negligible subset of the targeted pressure-temperature values. However, we verified in a few cases where the unscaled calculation converged, that the employed 0.1 scaling yielded minor quantitative differences in the thermal conductivity.

We also observed that solving the BTE in a too dense \mathbf{q} -point mesh could lead to an imaginary acoustic mode close to the critical pressure, because of inaccuracy of the Fourier interpolation in the calculation of the phonon bands. In order to avoid spurious effects due to such contributions we employed a slightly sparse \mathbf{q} -point mesh ($6 \times 6 \times 6$) so that no imaginary frequencies are sampled close to the critical pressure around the Γ point in the BZ integrations. Although the exact values of the conductivity are slightly underconverged with the \mathbf{q} -point grid and hence not quantitatively accurate, particularly close to the lattice thermal conductivity peak at each temperature, we have checked that our main qualitative results remain valid with denser grids.

Finally, we stress that all the results discussed in this work have been obtained by solving the BTE iteratively. Nevertheless, we have found that the RTA results for the lattice thermal conductivity differ at most by 10% in the whole (T, P) region we explored.

III. RESULTS

A. Phase transition under pressure

The crystal structure of the two silica polymorphs studied is shown in Figure 1. The stishovite phase belongs to the tetragonal crystal family with space group $P4_2/mnm$, while the CaCl_2 -type phase belongs to the orthorhombic crystal family with space group $Pnmm$. The latter differs from the former in a tilt of the oxygen octahedra surrounding the Si atoms and has lattice parameter $b \neq a$. We computed the relaxed lattice parameters and atomic positions of silica for pressures ranging from 0 to 100 GPa in both phases. In the stishovite phase we imposed $b = a$, while this restriction was lifted for

the CaCl_2 -type phase. The calculated a and b lattice parameters are shown in Figure 2, along with the oxygen octahedra rotation angle. At the critical pressure, a starts to differ from b , and the oxygen octahedra become tilted in the CaCl_2 -type phase.

This phase transition is known to be driven by the softening of the optical B_{1g} phonon mode in the BZ center, which corresponds precisely to a pure rotation of the oxygen octahedra. The critical pressure P_c is taken as that for which the dressed shear modulus $(c_{11} - c_{12})/2$ (where the c_{ij} is the ij component of the stiffness tensor in Voigt notation) vanishes in the stishovite phase, *i.e.*, the pressure at which the system shows no resistance to the shearing of the cell and the oxygen octahedra rotation. The computed shear modulus as a function of pressure is shown in Figure 2 (b). We obtain $P_c = 53.4$ GPa, in good agreement with previous calculations¹³ and experiments³⁶. This second-order phase transition is of the pseudoproper ferroelastic type, since the driving order parameter is not strain itself, but the strain emerging at the phase transition has the same symmetry as that order parameter^{13,21,37}.

Next, we compute the phonon band structure of silica in the stishovite and CaCl_2 -type phases at different pressures. Some representative cases of both phases are shown in Figure 3. We first note that some non-degenerate modes (such as the 3rd and 4th optical modes) of the CaCl_2 -type phase become degenerate in the stishovite phase due to the higher symmetry of silica in the tetragonal phase. Moreover, the phonon bands generally gain energy with increasing pressure, the only two exceptions being the lowest optical band around Γ (associated to the B_{1g} mode responsible for the structural phase transition), which softens close to $P = P_c$ and then gains energy together with the rest of the modes, and the lowest energy band in the high symmetry point A (S) in the stishovite (CaCl_2 -type) phase (see video in Supplemental Material at [URL]). For pressures between 25 and 70 GPa, one of the acoustic bands becomes imaginary in a small region of the BZ along the $\Gamma - M$ direction for the stishovite phase^{13,17}, and along the $\Gamma - S$ direction for the CaCl_2 -type phase. This artifact might be due to the finite supercell size employed in the calculations, since the relevant atomic interaction range is expected to increase as the system approaches the critical pressure, as pointed out in Ref. [13]. Thus, the calculation of the integrals in reciprocal space appearing in the BTE must be done with care, avoiding the small region where this acoustic band becomes imaginary so that no unphysical results are obtained.

B. Thermal conductivity

Solution of the BTE in the (T, P) space

We next solve the BTE for both silica phases for several values of temperature, T , and pressure, P . Figures 4

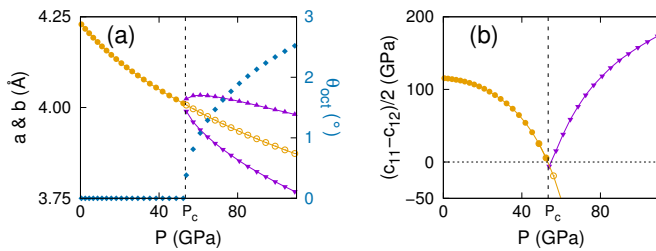


FIG. 2. (a) Lattice parameters a and b for SiO₂ as a function of pressure as obtained with DFT. Results for the stishovite phase are shown in orange (circles) while those for the CaCl₂-type phase are shown in purple (triangles). The rotation angle of the oxygen octahedron is shown with unconnected blue points. (b) Dressed shear modulus $\frac{(c_{11}-c_{12})}{2}$ as a function of pressure for the stishovite (orange) and CaCl₂-type (purple) phases. The shear modulus vanishes close to the phase transition.

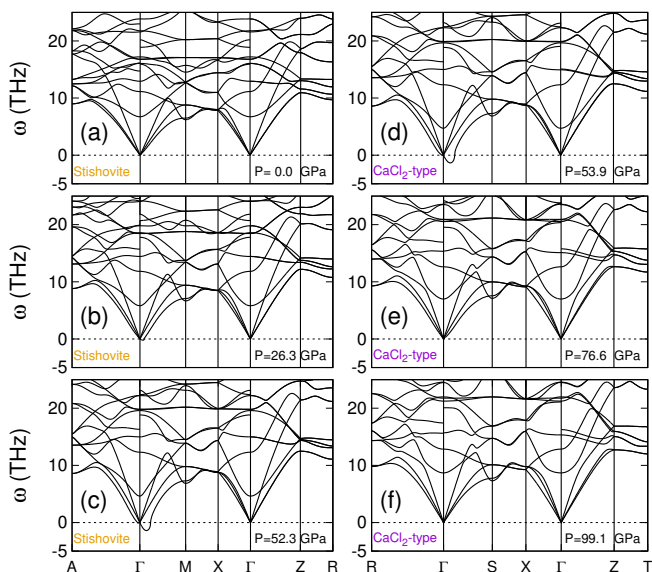


FIG. 3. Phonon band structure for three representative pressures of the stishovite phase –(a) to (c)– and the CaCl₂-type phase –(d) to (f)–. The modes have been computed for $P=0, 26.3, 52.3, 53.9, 76.6$ and 99.1 GPa.

(a) and (b) show the lattice thermal conductivity components κ^{zz} and κ^{xx} , respectively. We find that the off-diagonal components are negligible in the whole (T, P) space explored and that the κ^{yy} component (not shown) is equal to the κ^{xx} component in the stishovite phase due to symmetry. In the CaCl₂-type phase κ^{yy} shows a similar behavior to κ^{xx} . For pressures below (above) the critical pressure we only show the results for the stishovite (CaCl₂-type phase), *i.e.*, only the results for the stable phase at each pressure are shown. We first note that both components are substantially different in most of the (T, P) space. More importantly, we find an astonishingly large peak in κ^{xx} close to the critical pressure at both sides of the critical line for temperatures between 8 and 70 K.

In Figure 4 (c) we show the lattice thermal conductivity for the $P=76.6$ GPa isobar. We find the characteristic trend of the lattice thermal conductivity curves for bulk systems. At low temperatures κ increases with T until it reaches a maximum, after which the conductivity decreases more slowly. We also note that κ^{xx} is almost equal to κ^{yy} in the whole temperature range, while κ^{zz} is smaller below $T=200$ K. Thus, the thermal response of silica is clearly anisotropic in general.

In Figure 5 we show κ^{xx} profiles for different isotherms. The lattice thermal conductivity close to $P = P_c$ increases up to 2 orders of magnitude for low temperatures (see the $T=10$ K line in Fig. 5), and about 1 order of magnitude for medium temperatures (see the 40 K isotherm in the same figure). At higher temperatures, at which the scattering is dominated by anharmonic processes, the peak is smoothed out until it disappears (see the 100 K and 300 K isotherms). This suggests that the peak stems from a shift in the dominant scattering processes, from isotopic to anharmonic phonon-phonon, as temperature increases (recall that we are calculating the bulk lattice thermal conductivity, thus ignoring boundary scattering processes). This can be confirmed, for example, by re-computing the thermal conductivity maps $\kappa(T, P)$ with no anharmonic scattering. Since isotopic scattering is dominant at low temperatures, we obtained almost identical results for $T < 100$ K, while at each pressure $\kappa(T)$ saturates to a constant value for $T \gtrsim 150$ K.

Origin of the peak around the critical pressure

In order to trace the origin of the notorious peak in the in-plane thermal conductivity, we analyze the contribution to κ^{xx} of each mode in each of the sampled points in the BZ. The individual contributions of all the modes included in our BZ integrations at different representative temperatures and pressures are depicted in Figure 6. For each \mathbf{q} -point in the irreducible BZ the contribution of the 18 modes is shown. At $T=40$ K (upper row in the Figure), we see that κ^{xx} is strongly dominated by the contribution of a few low energy modes. Also, one (degenerate) mode contributes with up to $2.7 \cdot 10^3 \text{ W m}^{-1} \text{ K}^{-1}$ for $P \approx P_c$ but is not so active at high or low pressures. For higher temperatures ($T=100$ K and $T=300$ K, second and third rows in the Figure respectively), although the dominant contributions still correspond to low energy modes, optical phonons start to play an increasingly important role in the total thermal conductivity. Furthermore, the general trend is a monotonic increase of the individual contributions with increasing pressure. In this way, we can attribute the peak in the in-plane lattice thermal conductivity at low temperatures to the enhancement of the contribution of particular low energy acoustic modes.

We now analyze the evolution of the individual contributions κ_{λ}^{xx} with pressure. The results for two representative temperatures (10 and 300 K) are shown in Fig-

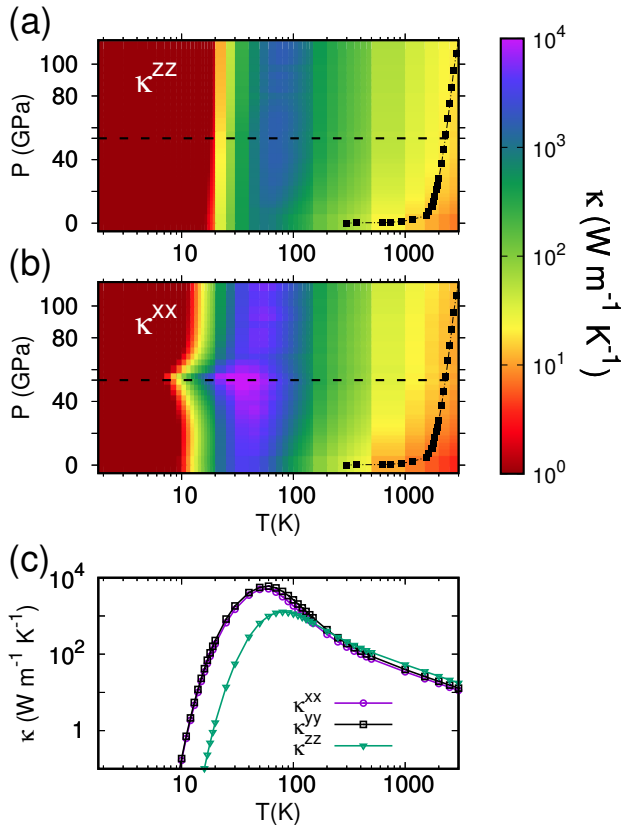


FIG. 4. Lattice thermal conductivity of SiO₂ for different pressures and temperatures (see color code on the right). The zz component of the lattice thermal conductivity is shown in (a), and the xx component in (b). The results for the stishovite phase are shown only for pressures below P_c , while the results for the CaCl₂-type phase are displayed above P_c . The zz component shows a slight increase as pressure increases, but no special feature is seen at $P = P_c$. The xx component, is larger than the zz one for $T < 200$ K, showing a huge enhancement around the critical pressure for temperatures below 40 K. Dotted dashed black curves show the average geotherm according to Dziewonski and Anderson's Earth model³⁸. (c) Lattice thermal conductivity along the $P=76.6$ GPa isobar. Purple circles, black squares, and green triangles correspond to the xx , yy , and zz components, respectively.

ure 7. The total κ^{xx} is also presented with black filled circles for comparison. On the one hand, at $T=10$ K thermal transport is dominated by essentially one mode –purple squares in the Figure, mode (I)– for pressures between 30 and 60 GPa (see that the total κ^{xx} is almost equal to the contribution of this mode in this pressure range). The aforementioned mode is a low energy acoustic phonon with wavevector $\mathbf{q} = (1/6, 1/6, 0)$ in reciprocal vector units, which is representative of an entire region of low energy modes close to the BZ center. Away from this pressure window, the contribution of another acoustic mode –mode (II)– with $\mathbf{q} = (1/3, 0, 0)$ in reciprocal vector units (green squares) becomes larger than that of mode (I), hence dominating the thermal conductivity at

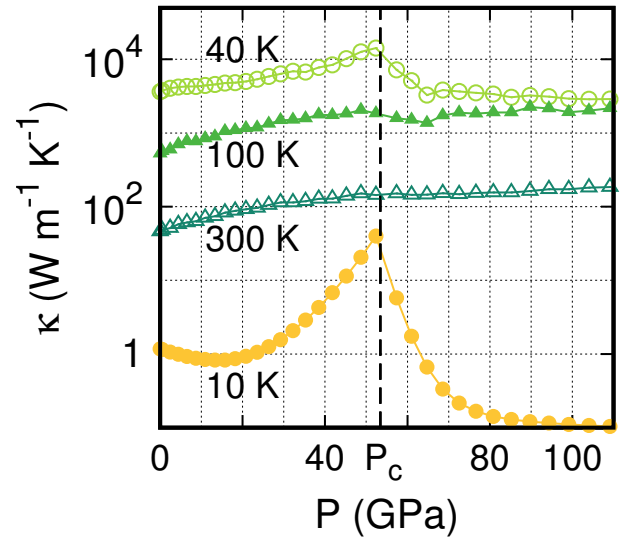


FIG. 5. Constant temperature profiles of κ^{xx} as a function of pressure, for $T=10$ K (filled circles), $T=40$ K (empty circles), $T=100$ K (filled triangles) and $T=300$ K (empty triangles).

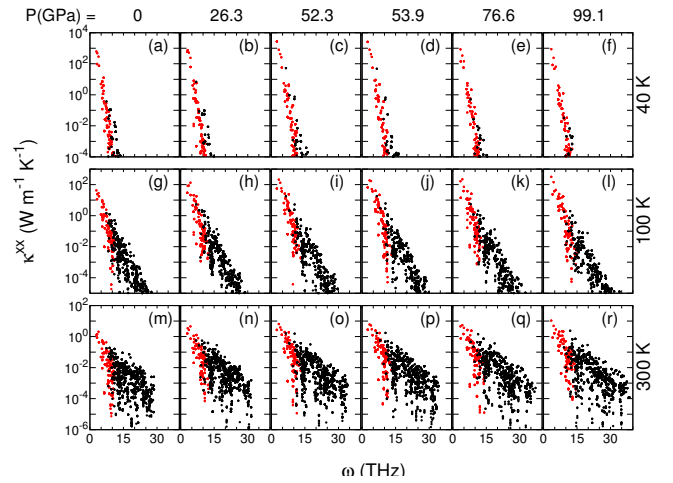


FIG. 6. Contribution to the total lattice thermal conductivity for each mode λ (κ_λ). The first, second and third rows correspond to calculations at $T=40$, 100 and 300 K respectively. The columns from left to right correspond to $P=0$, 26.3, 52.3, 53.9, 76.6 and 99.1 GPa, where the results are shown only for the stable phase at each pressure. Close to the critical pressure, a few acoustic modes are responsible for the anomalously large value of κ^{xx} at $T=40$ K –(c) and (d)–. For $T=100$ K –(g) to (l)– and $T=300$ K –(m) to (r)–, there is no peak in κ^{xx} at $P = P_c$ and the κ_λ of the highest contributing modes increases monotonically with pressure. Red (black) dots correspond to acoustic (optical) modes.

low and high pressures. The contribution of the next highest contributing mode is about one order of magnitude smaller, thus thermal transport in silica close to the phase transition is strongly governed by the behavior of the acoustic phonons represented by mode (I). On the other hand, at $T=300$ K many modes give contri-

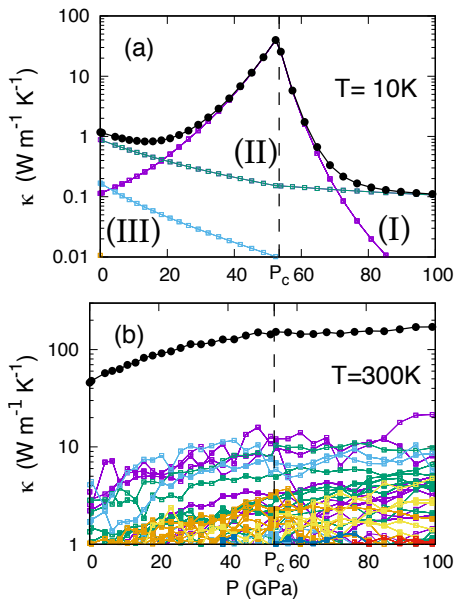


FIG. 7. Contribution to κ^{xx} as a function of pressure of the different modes for (a) $T=10$ K and (b) $T=300$ K. The total thermal conductivity at each temperature is shown in black circles.

contributions in the range of 1 to 10 $\text{W m}^{-1}\text{K}^{-1}$. The total κ^{xx} is thus the addition of many contributions of similar magnitude, and no particular mode dominates the thermal transport properties of SiO_2 in the studied pressure range. Moreover, there is only a minor dip in the total thermal conductivity close to the critical pressure, and this feature can not be attributed to an individual mode. Although the overall thermal conductivity increases almost monotonically with pressure, not all of the highly contributing modes follow this behavior.

With the aim of acquiring some deeper insight of the origin of the peak, we now analyze the different factors that determine the contribution of mode (I) and its evolution with pressure. Figure 8 shows the evolution with pressure of the main different factors involved in $\kappa_{(I)}^{xx}$, namely the isotopic scattering rate, the square of the frequency, the product of populations $n_{(I)}^0(n_{(I)}^0+1)$ and the group velocity –see Eq. (5)–. While the term $\omega_{(I)}^2$ decreases by a factor of 0.6 at the critical pressure (with respect to $P=0$), the remaining pressure dependent factors increase as the pressure approaches P_c . In fact, a decreasing ω_{λ}^2 is always overcompensated by the growth of $n_{\lambda}^0(n_{\lambda}^0+1)$, *i.e.*, the softening of a phonon band results in a larger contribution to the thermal conductivity (not taking into account the possible changes in the relaxation times). The largest ratio for mode (I) is precisely that of the phonon population product $n_{\lambda}^0(n_{\lambda}^0+1)$, which accounts for a factor of 33.5 in the enhancement close to the critical pressure. The isotopic scattering rate (which at low temperatures is much larger than the anharmonic scattering rate) decreases by a factor of 6, increasing the contribution of mode (I) to the thermal conductivity by

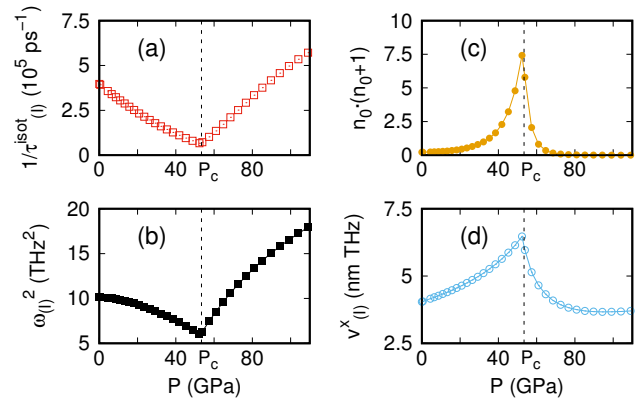


FIG. 8. Evolution of isotopic scattering rate of mode (I), squared frequency of mode (I), $n_0(n_0+1)$ at $T=10$ K for mode (I) and x component of the group velocity of mode (I) with pressure –(a), (b), (c) and (d) respectively–. The critical pressure P_c is indicated with a vertical dashed line as a guide to the eye in all cases.

the same factor and being this the second largest ratio. The decrease in the unit cell volume and the increase in group velocity close to P_c contribute to the total ratio with factors of 1.1 and 2.6 respectively.

Therefore, we find that the computed large enhancement of the in-plane lattice thermal conductivity at low temperatures is caused by the contribution of a single mode, representative of a region of soft acoustic vibrations close to the Γ point. We have further analyzed the evolution with pressure of the different factors that affect the individual contribution of the mode responsible for the peak, finding that, while the frequency of mode (I) has a minimum close to $P=P_c$, this alone enhances the contribution to the low-temperature lattice thermal conductivity since the mode becomes highly populated. The remaining factors also contribute to the enhancement of κ^{xx} to a lesser extent. On the other hand, at higher temperatures the softest modes are highly populated regardless of the pressure, and anharmonic scattering becomes dominant, so that no peak is found at the critical point.

Thermal conductivity of SiO_2 along the geotherm

The thermal conductivity of the Earth’s mantle determines its convection mechanism and the heat budget of our planet⁶. Owing to the great interest of SiO_2 in the field of geophysics, we additionally computed the thermal conductivity tensor of silica along an average geotherm³⁸ from the Earth’s crust up to depths of 2400 km, deep inside the lower mantle. The results are displayed in Figure 9. We first note that for high temperatures the anisotropy is reversed, being κ^{zz} larger than κ^{xx} and κ^{yy} , as opposed to the results analyzed above for lower tem-

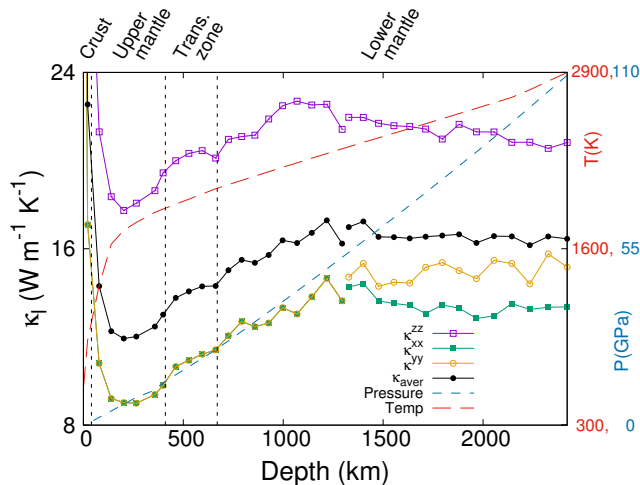


FIG. 9. Lattice thermal conductivity of silica in the stishovite and CaCl_2 -type phases along an average geotherm. The results for the stishovite (CaCl_2 -type) phase are shown for $P < (>)P_c$, and the phase transition is marked by a discontinuity in the lattice thermal conductivity lines. Filled squares, empty circles and empty squares correspond to the diagonal components κ^{xx} , κ^{yy} and κ^{zz} respectively, and the average lattice thermal conductivity $\kappa_{\text{aver}} = \frac{1}{3}(\kappa^{xx} + \kappa^{yy} + \kappa^{zz})$ is shown with filled circles (see legend). The average estimated temperature (pressure) at each depth from the Earth's crust is shown with a long-(short-)dashed red (blue) line. There is a marked decrease in the three diagonal components of κ close to $P = P_c$.

peratures. In the stishovite phase, the three diagonal components increase approximately linearly with depth up to the critical pressure, while for the CaCl_2 -type phase the thermal conductivity is roughly constant with depth. Nevertheless, an abrupt decrease in all the components is seen close to the phase transition, which is marked by a discontinuity in the lines in the Figure. Interestingly, we note that in a work by Murphy *et al.* on PbTe-based materials³⁹ a dip in the thermal conductivity of ferroelectric compounds was also predicted close to a structural phase transition.

These results suggest that the marked decrease in κ close to the phase transition could be used as a geophysical signature to distinguish stishovite-rich regions from CaCl_2 -type-rich regions in the Earth's interior, and thus as an indirect measure of the pressure and the conditions therein.

C. Discussion

The present work was partly motivated by our conjecture that SiO_2 should be a suitable model compound to investigate changes in thermal conductivity across a soft-mode-driven structural phase transition. Indeed, it seemed to us that SiO_2 's transformation between the stishovite and CaCl_2 -type structures might be representative of other soft-mode ferroelastic (and ferroelec-

tric) transitions, with the advantage that the transition-controlling parameter (pressure, as opposed to temperature) is trivial to handle in a first-principles simulation. Hence, let us briefly discuss the generality of our findings for SiO_2 , and whether our initial conjecture was correct.

Most importantly, our simulations predict that SiO_2 will display some strong changes in its low-temperature thermal conductivity around the transition pressure. Interestingly, such features are not directly related with the optical soft mode itself, which is the primary order parameter for the transformation but has a negligible impact in κ . Instead, they can be traced back to the accompanying softening of an acoustic band, an effect that is specific to the peculiar pseudoproper ferroelastic character of the investigated transition in SiO_2 . Hence, this suggests that enhancements of the low-temperature conductivity, as those we observed in SiO_2 , can be expected to occur at ferroelastic transitions involving a significant softening of the acoustic bands. Our results also suggest that, in contrast, other soft mode transformations – as, *e.g.*, ferroelectric or anti-ferrodistortive transitions in which only an optical bands softens – will in general not present such marked effects in the thermal conductivity.

Additionally, our results show that, in SiO_2 , significant changes in the lattice thermal conductivity are restricted to relatively low temperatures. More precisely, we find that, while the softening of the key acoustic band causes a large increase in its population at low temperatures – Fig. 8 (c) –, the relative population change is small at higher values of T ; as a result, the effect in the conductivity at higher temperatures is modest as well. Naturally, we do not know whether, in other materials, phonon frequencies and populations will control the variations of κ to the same extent that we find they do in SiO_2 . Yet, it is clear that, unlike the material-specific scattering rates or group velocities in Eq. (5), temperature-dependent populations are governed by universal laws. Hence, our results suggest that, generally speaking, changes in the conductivity associated to the softening of phonon bands will be restricted to low temperatures. Hence, in what regards applications at ambient conditions, it seems dubious that we can take advantage of effects associated to soft-mode-driven phase transitions.

IV. CONCLUSIONS

By means of state-of-the-art calculations, we have characterized the stishovite and CaCl_2 -type high pressure phases of silica and computed a thermal conductivity map $\kappa(T, P)$ for a large number of points in the (T, P) space. We found that, for pressures close to the phase transition, a large peak in the in-plane conductivity appears at both sides of the phase transition and at T below 70 K. Moreover, this peak is not present in the out-of-plane conductivity, thus leading to a highly anisotropic thermal material. We have tracked down the origin of this unexpected peak, and found that it originates in

the softening of an acoustic band that becomes highly populated close to the phase transition. We have discussed the general implications of our results, which suggest that lattice thermal conductivity effects associated to soft-mode transitions will be restricted to low temperatures and, thus, may not be promising for applications at ambient conditions. Finally, we have computed the thermal conductivity along an average geotherm for its possible applications in the field of geophysics, since SiO_2 is the most abundant compound in the Earth's mantle.

ACKNOWLEDGMENTS

We acknowledge financial support by the Ministerio de Economía, Industria y Competitividad (MINECO) under grant FEDER-MAT2013-40581-P and the Severo Ochoa Centres of Excellence Program under grant SEV-2015-0496, and by the Generalitat de Catalunya under grant no. 2014 SGR 301. We also acknowledge the financial support of the Luxembourg National Research Fund (Grant FNR/P12/4853155/Kreisel COFERMAT). We acknowledge the use of computational resources of CESGA, and the i2BASQUE academic network. Finally, we acknowledge Prof. Robert T. Downs for pointing to Reference [38].

-
- ¹ G. Mahan, *APL Materials* **4**, 104806 (2016).
- ² G. Chen, *Nanoscale energy transport and conversion: a parallel treatment of electrons, molecules, phonons, and photons* (Oxford University Press, 2005).
- ³ T. Luo and G. Chen, *Physical Chemistry Chemical Physics* **15**, 3389 (2013).
- ⁴ A. Roy, *Phys. Rev. B* **93**, 100101 (2016).
- ⁵ S. Stackhouse, L. Stixrude, and B. B. Karki, *Phys. Rev. Lett.* **104**, 208501 (2010).
- ⁶ X. Tang and J. Dong, *Proceedings of the National Academy of Sciences* **107**, 4539 (2010).
- ⁷ X. Tang, M. C. Ntam, J. Dong, E. S. G. Rainey, and A. Kavner, *Geophysical Research Letters* **41**, 2746 (2014).
- ⁸ J. W. Morgan and E. Anders, *Proceedings of the National Academy of Sciences* **77**, 6973 (1980).
- ⁹ O. Kuskov, *Physics of the Earth and Planetary Interiors* **102**, 239 (1997).
- ¹⁰ R. Rieder, T. Economou, H. Wänke, A. Turkevich, J. Crisp, J. Brückner, G. Dreibus, and H. McSween, *Science* **278**, 1771 (1997).
- ¹¹ M. A. Spackman, R. J. Hill, and G. V. Gibbs, *Physics and Chemistry of Minerals* **14**, 139 (1987).
- ¹² D. M. Teter, R. J. Hemley, G. Kresse, and J. Hafner, *Phys. Rev. Lett.* **80**, 2145 (1998).
- ¹³ A. Togo, F. Oba, and I. Tanaka, *Physical Review B* **78**, 134106 (2008).
- ¹⁴ Y. Tsuchida and T. Yagi, *Nature* **340**, 217 (1989).
- ¹⁵ R. E. Cohen, "First-principles predictions of elasticity and phase transitions in high pressure SiO_2 and geophysical implications," in *High-pressure Research: Application to Earth and Planetary Sciences* (American Geophysical Union, 1993) pp. 425–431.
- ¹⁶ A. R. Oganov, M. J. Gillan, and G. D. Price, *Phys. Rev. B* **71**, 064104 (2005).
- ¹⁷ T. Tsuchiya, R. Caracas, and J. Tsuchiya, *Geophysical Research Letters* **31**, L11610 (2004).
- ¹⁸ J. R. Alvarez and P. Rez, *Solid State Communications* **108**, 37 (1998).
- ¹⁹ D. Li, G. Bancroft, M. Kasrai, M. Fleet, R. Secco, X. Feng, K. Tan, and B. Yang, *American Mineralogist* **79**, 622 (1994).
- ²⁰ A. Soldatov, M. Kasrai, and G. Bancroft, *Solid State Communications* **115**, 687 (2000).
- ²¹ M. A. Carpenter, R. J. Hemley, and H.-k. Mao, *Journal of Geophysical Research: Solid Earth* **105**, 10807 (2000).
- ²² M. A. Carpenter, *American Mineralogist* **91**, 229 (2006).
- ²³ D. Andrault, G. Fiquet, F. Guyot, and M. Hanfland, *Science* **282**, 720 (1998).
- ²⁴ G. Kresse and J. Hafner, *Phys. Rev. B* **48**, 13115 (1993).
- ²⁵ G. Kresse and J. Furthmüller, *Computational Materials Science* **6**, 15 (1996).
- ²⁶ J. P. Perdew, K. Burke, and M. Ernzerhof, *Phys. Rev. Lett.* **77**, 3865 (1996).
- ²⁷ P. E. Blöchl, *Physical Review B* **50**, 17953 (1994).
- ²⁸ G. Kresse and D. Joubert, *Physical Review B* **59**, 1758 (1999).
- ²⁹ H. J. Monkhorst and J. D. Pack, *Physical Review B* **13**, 5188 (1976).
- ³⁰ A. Togo and I. Tanaka, *Scripta Materialia* **108**, 1 (2015).
- ³¹ W. Li, J. Carrete, N. A. Katcho, and N. Mingo, *Computer Physics Communications* **185**, 1747 (2014).
- ³² S.-I. Tamura, *Phys. Rev. B* **27**, 858 (1983).
- ³³ R. C. Weast, M. J. Astle, W. H. Beyer, *et al.*, "CRC Handbook of Chemistry and Physics," (1988).
- ³⁴ I. Pomeranchuk, *Phys. Rev.* **60**, 820 (1941).
- ³⁵ M. Omini and A. Sparavigna, *Physica B: Condensed Matter* **212**, 101 (1995).
- ³⁶ K. J. Kingma, R. E. Cohen, R. J. Hemley, and H.-k. Mao, *Nature* **374**, 243 (1995).
- ³⁷ V. Wadhawan, *Introduction to ferroic materials* (CRC press, 2000).
- ³⁸ A. M. Dziewonski and D. L. Anderson, *Physics of the Earth and planetary interiors* **25**, 297 (1981).
- ³⁹ R. M. Murphy, E. D. Murray, S. Fahy, and I. Savić, *Phys. Rev. B* **93**, 104304 (2016).